Novel Technique for In-Body Absorbed Power Density Assessment Based on Free-Space E-Field Measurement

Massinissa Ziane, Artem Boriskin, Cécile Leconte, L. Le Coq, Maxim Zhadobov

Novel Technique for In-Body Absorbed Power Density Assessment Based on Free-Space *E*-Field Measurement

Massinissa Ziane, Artem Boriskin, *Senior Member, IEEE*, Cecile Leconte, Laurent Le Coq, *Senior Member, IEEE*, and Maxim Zhadobov, *Senior Member, IEEE*

***Abstract*— We introduce a novel method for measurement of the absorbed power density (APD) above 6 GHz, accounting for antenna/body interaction. A reflectivity-based thin planar solid phantom is used to mimic the scattering characteristics of human skin. This allows to perturb the antenna under test (AUT) in a similar way as it would be perturbed by the presence of the human body. The lower electromagnetic losses in the phantom medium result in an enhanced transmission through the phantom facilitating free-space *E*-field vector measurement on the opposite to the AUT side of the phantom. The measured *E*-field is backpropagated in space to retrieve APD using a plane-wave spectrum (PWS) technique. The proposed method is validated at 60 GHz using reference antennas, namely, a cavity-fed dipole array and pyramidal horn with a slot array. A very good agreement is demonstrated between the target APD at the air/skin interface (peak, averaged, and spatial distribution) and the one reconstructed from the simulated and measured *E*-field. The maximum relative deviations between the computed and measured peak (pAPD), 1 cm^2 peak spatial average ($ps\text{APD}_{1\,\text{cm}^2}$), and 4 cm^2 peak spatial average ($ps\text{APD}_{4\,\text{cm}^2}$) are 13.2% (0.55 dB), 14.9% (0.6 dB), and 15.7% (0.63 dB), respectively. The results demonstrate that the proposed technique is promising for experimental dosimetry and compliance testing of wireless devices operating above 6 GHz.**

***Index Terms*— Absorbed power density (APD), dosimetry, millimeter waves (mmWaves), near-field measurements.**

NOMENCLATURE

$\boldsymbol{E}$	E-field vector.
$\hat{\boldsymbol{E}}$	PWS of $\boldsymbol{E}$ vector.
$\boldsymbol{E}_0$	$\boldsymbol{E}$ at phantom surface ($z = 0$).
$\boldsymbol{E}_p$	$\boldsymbol{E}$ at the scanning plane ($z = s + d_p$).
$\boldsymbol{E}_{(p,s)}$	Simulated $\boldsymbol{E}_p$ (without OWG probe).
$\boldsymbol{E}_{(p,m)}$	Measured absolute $\boldsymbol{E}_p$.
$\boldsymbol{E}_{(p,r,m)}$	Measured relative $\boldsymbol{E}_p$.
$\boldsymbol{E}_{(\text{ref},s)}$	Simulated reference $\boldsymbol{E}$ (without OWG probe).
$\boldsymbol{E}_{(\text{ref},m)}$	Measured reference $\boldsymbol{E}$.
$\boldsymbol{M}_c$	Probe calibration matrix.
$\boldsymbol{H}$	H-field vector.
$\text{APD}_{(s)}$	Simulated APD at the surface of the skin.
$\text{APD}_{(r,s)}$	Reconstructed APD from $\boldsymbol{E}_{(p,s)}$.
$\text{APD}_{(r,m)}$	Reconstructed APD from $\boldsymbol{E}_{(p,m)}$.
pAPD	Peak APD.
sAPD	Spatial average APD.
psAPD	Peak spatial average APD.
Δ_i^j	Relative error on reconstructed APD.
Δ_s^j	Relative error on $\text{APD}_{(r,s)}$.
Δ_m^j	Relative error on $\text{APD}_{(r,m)}$.
Υ	Correlation factor.
ϵ_r	Complex relative permittivity of the phantom.
k_0	Free-space propagation constant.
k_d	Propagation constant in the phantom.
k_z	Longitudinal propagation constant.
k_z^0	Longitudinal propagation constant in the air.
k_z^d	Longitudinal propagation constant in the phantom.
λ_0	Free-space wavelength.
λ_d	Wavelength in the phantom.
$\boldsymbol{T}$	Spectral transmission coefficient.
$\boldsymbol{R}$	Spectral reflection coefficient.
s	Phantom thickness.
d	Distance between AUT and phantom.
d_p	Distance between phantom and probe.

Manuscript received 4 September 2023; revised 7 November 2023; accepted 20 November 2023. This work was supported in part by the French National Research Program for Environmental and Occupational Health of Agence Nationale de Sécurité Sanitaire de l'alimentation, de l'Environnement et du travail (ANSES) through NEAR 5G Project under Grant 2018/2 RF/07; in part by the Labex CominLabs through EM-ART Project under Grant ANR-10-LABX-07-01; in part by the "Région Bretagne" (ARED Program); in part by the French Ministry of Higher Education and Research (MESR); in part by the Brittany Region, Ministry of Higher Education and Research, Rennes Métropole and Conseil Départemental through CPER Project SOPHIE/STIC and Ondes; and in part by the French National Center for Scientific Research (CNRS). *(Corresponding author: Massinissa Ziane.)*

The authors are with the University of Rennes, CNRS, Institut d'Electronique et des Technologies du numéerique (IETR), UMR 6164, 35042 Rennes, France (e-mail: massinissa.ziane@univ-rennes.fr; maxim.zhadobov@univ-rennes.fr).

Color versions of one or more figures in this article are available at https://doi.org/10.1109/TMTT.2023.3336798.

Digital Object Identifier 10.1109/TMTT.2023.3336798

I. INTRODUCTION

THE continuous evolution of mobile terminals, such as smartphones, tablets, and body-worn devices, has drastically increased the wireless data traffic, which keeps growing due to video streaming applications and cloud computing. The growing need for high-performance mobile communications leads to a progressive shift of operating frequencies toward the millimeter-wave (mmWave) band. In particular, the fifth-generation (5G) heterogeneous cellular mobile networks will

exploit the FR2 bands around 26 GHz, 39 GHz, and in some countries 60 GHz [1], [2], [3], [4], [5].

The upcoming use of FR2 technologies will involve user exposure to mmWave radiation. This includes the near-field exposure by mobile devices operating in the vicinity of human body. mmWave radiation is not present in our natural background due to the strong atmospheric absorption, and the accurate control of user exposure is of upmost importance from the environmental safety viewpoint. To prevent overexposure risks, safety exposure limits are set by the International Commission on Non-Ionizing Radiation Protection (ICNIRP) and the Institute of Electrical and Electronics Engineering (IEEE C95.1) [6], [7].

Below 6 GHz, the specific absorption rate (SAR) is used as the main dosimetric quantity. Above 6 GHz and up to 300 GHz, in-tissue power density at the skin surface, referred as the absorbed power density (APD) by ICNIRP and as the epithelial power density by IEEE C95.1, is used as the main dosimetric quantity. The limits (basic restrictions) are set to 10 mW/cm^2 for occupational environments (referred as restricted environments by IEEE) and 2 mW/cm^2 for the general public (referred as unrestricted environments by IEEE). The APD is to be averaged over 4 cm^2 and 6 min. To account for focal beam exposure, from 30 to 300 GHz APD is also to be averaged over 1 cm^2 and must not exceed two times the limits for 4 cm^2. Note that the algorithms for APD averaging in compliance testing are currently under discussion [8], [9].

Compliance testing of wireless devices with respect to the exposure limits is currently performed based on free-space measurement of the incident power density (IPD) close to a device under test according to the IEC/IEEE 63195 standard [10]. In [11], IPD is assessed using a miniaturized diode-loaded probe designed to measure the magnitude of the E-field deriving the polarization ellipse from different probe rotation angles. The phase, which cannot be directly measured by such probes, is retrieved using the plane-to-plane phase reconstruction method [12]. It consists in: 1) amplitude measurement in two parallel planes at different distances from the source (the phase distribution is arbitrary set in both the planes) and 2) iterative forward and backward near-field to near-field transformation until the phase distribution converges.

For accurate exposure assessment under realistic conditions, it is important to account for antenna/body interaction, including standing wave and antenna detuning phenomena that may result in enhancement of user exposure levels [13], [14]. To account for this, the microwave dosimetry methods, based on in-phantom E-field measurements of SAR, are commonly used below 10 GHz. However, at higher microwave frequencies they are facing physical limitations due to prohibitively high losses in biological tissues [15], [16], [17], [18]. This substantially complicates measurement of the transmitted E-field using a scanning probe (or an embedded array of probes) inside a tissue-simulating liquid. Some attempts have been undertaken to scale the in-phantom measurement methods to frequencies above 10 GHz [19], [20], [21], [22]. The vector E-field is probed inside the liquid phantom and then backpropagated in space to retrieve APD at the phantom surface. As an alternative, a temperature-based method for APD assessment was proposed in [23], [24], and [25] to allow APD retrieval from the mmWave-induced temperature rise on the phantom surface measured using an infrared (IR) camera with the spatial resolution of the order of 100 μm.

This article introduces a novel technique for APD assessment based on free-space E-field measurements, accounting for antenna/body interaction. The method uses a reflectivity-based thin planar solid phantom designed to mimic the scattering characteristics of human skin and maximize the through-phantom transmission to guarantee a measurable E-field behind the phantom. A tapered open-ended waveguide is used as a probe to measure the amplitude and phase of the transmitted E-field. Free-space measurements ensure enhanced robustness with respect to probe positioning compared with the measurements in lossy liquid phantoms with a strong spatial APD gradient. The measured E-field is then backpropagated in space to retrieve APD at the phantom surface using a plane-wave spectrum (PWS) technique. The method is experimentally validated at 60 GHz using a near-field scanner for two reference feeds: a cavity-fed dipole array and a pyramidal horn with slot array [10].

II. Method Overview

The proposed APD assessment method is schematically represented in Fig. 1. The antenna under test (AUT) is placed at a distance d from a thin phantom reproducing the scattering properties of human skin. This reflectivity-based phantom, described in Section II-A, perturbs the AUT in the same way as it would be perturbed by the presence of the human body [23], [24]. Note that the complex permittivity of the phantom is different from the one of skin. It is chosen to reduce the losses in the phantom medium and thus enhance transmission through the phantom and ensure measurable E-field tangential component ($\boldsymbol{E}_p^{||}$) at $z > s$. $\boldsymbol{E}_p^{||}$ is sensed using a free-space probe at $z = s + d_p$ where s is the phantom thickness and d_p is the distance between the phantom and the probe. Using the PWS theory [26], $\boldsymbol{E}_p^{||}$ is backpropagated in the negative z-direction to retrieve the E-field ($\boldsymbol{E}_0$) and then APD at $z = 0$ (as detailed in Section II-B). The accuracy of the reconstruction technique is numerically assessed as detailed in Section II-C.

A. Reflectivity-Based Skin-Equivalent Phantom

At mmWaves, skin is characterized by relatively high dielectric losses ($\epsilon_r = 7.98 - j11.90$ at 60 GHz [27]). In phantoms reproducing the complex permittivity of skin, and therefore simulating both the absorption and scattering properties of skin, the electromagnetic power is absorbed at the phantom surface (penetration depth is about 0.5 mm at 60 GHz). The shallow penetration at mmWaves complicates the APD reconstruction from E-field measurement inside a lossy liquid phantom.

To overcome this problem, an alternative approach consists in using a thin phantom reproducing the power reflection coefficient of skin (i.e., ≈37.6% for the normal incidence,

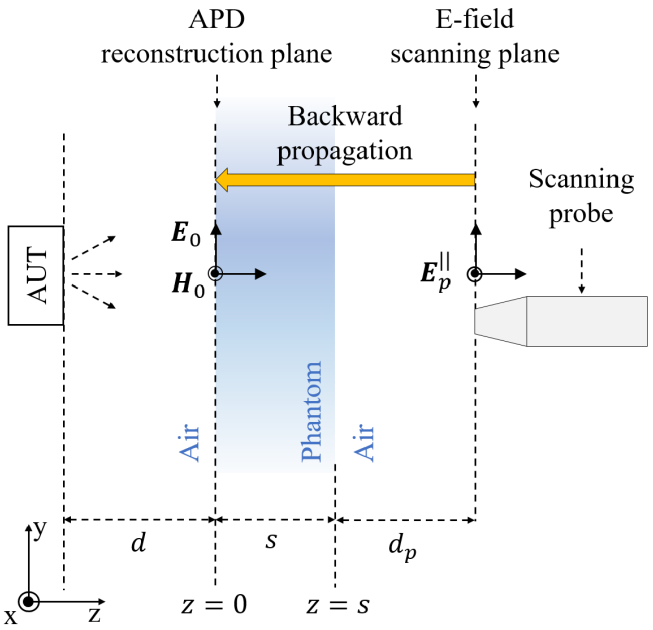

Fig. 1. Schematic representation of the proposed APD assessment method from free-space *E*-field vector measurement.

Gabriel's dry skin model [27] at 60 GHz). Such thin electromagnetic skin phantom, initially introduced in [28], reproduces the antenna/body interaction thus ensuring realistic measurements representative of close-to-body use cases. According to the power conservation principle, the APD at $z = 0$ is equal to the one at the skin surface since the reflected from the phantom power is the same as the power reflected from skin (within the measurement accuracy). Note that the single-layer phantom is enough for accurate APD evaluation, and introducing additional tissue layers would unnecessarily overcomplicate the phantom design and substantially complicate its fabrication, introducing additional sources of uncertainty. To ensure a measurable amplitude and phase of *E*-field in the scanning plane located at the opposite of the AUT side (Fig. 1), the complex permittivity and thickness of the phantom are jointly adjusted to minimize losses inside and maximize the through-phantom transmission.

The phantom is fabricated using carbon black powder and PDMS [Fig. 2(a)] as detailed in [28]. The dimensions of the phantom are chosen to be large enough to avoid surface waves (10 × 10 cm corresponding to 20 × 20λ_0, where λ_0 is the free-space wavelength). In brief, the PDMS and carbon powder are mixed and stirred thoroughly, then degassed under vacuum, and finally dried in an oven at 110 °C. For the carbon concentration of 40%, the optimal phantom thickness was found to be 1.2 mm. The complex permittivity of the carbon-PDMS mixture was measured using the free-space transmission method [28]. It uses a vector network analyzer (VNA), a transmission/reflection quasi-optical setup with two focusing lenses, and two reference WR-15 horn antennas. The measured complex permittivity of the phantom bulk material at 60 GHz is $\epsilon_r = 12.5 - j3.6$.

The power reflection coefficient transmitted through the phantom power was calculated at 60 GHz using Fresnel equations [Fig. 2(b) and (c)] [29]. The power reflection coefficient and transmitted through the phantom power were calculated was 36.6% for the normal incidence, which is

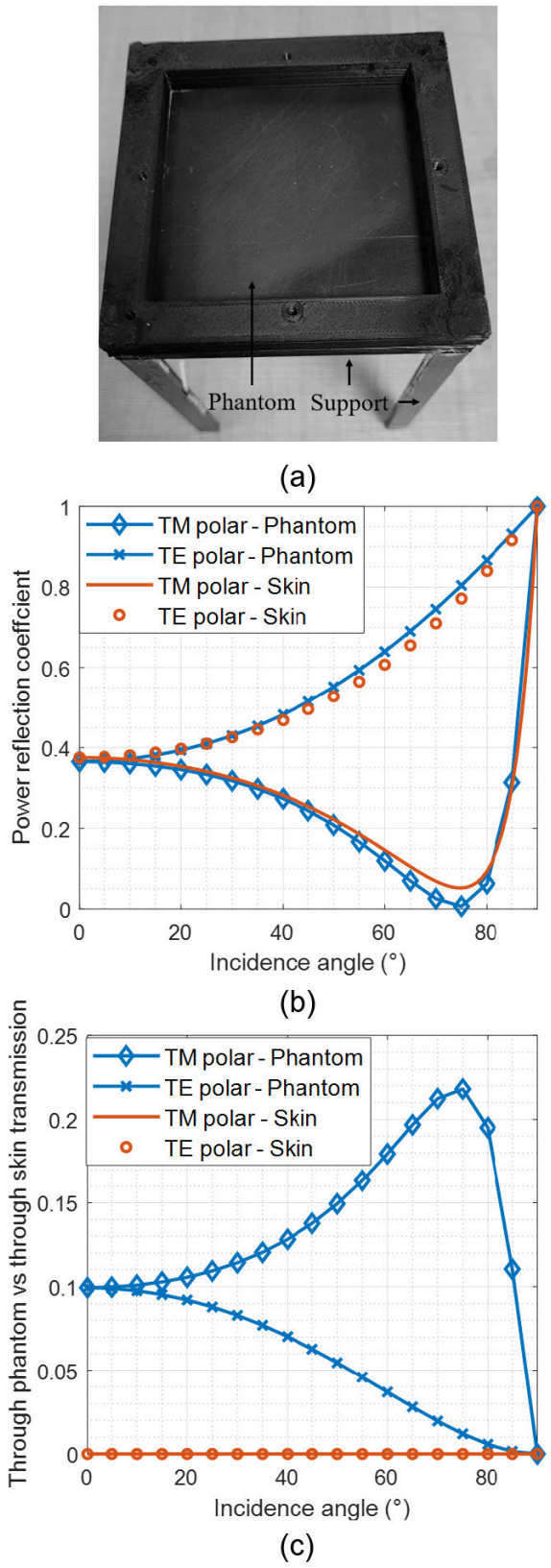

Fig. 2. Reflectivity-based phantom. (a) Fabricated prototype. (b) Power reflection coefficient versus incident angle for parallel (TM) and perpendicular (TE) polarizations. (c) Through phantom versus through skin power transmission for normal incidence at 60 GHz (normalized to the incident power).

in excellent agreement with Gabriel's dry skin model (<1% deviation). The maximum difference of 2% is found for the 0°–45° range, which implies that APD at the air/phantom interface is the same as at the air/skin interface (with discrepancy less than 4%) according to the power conservation principle. The power transmission through the phantom is 9.94% at the normal incidence. It is 29× higher compared with the skin-equivalent model with the same thickness. Accounting for APD exposure limits (2 and 4 mW/cm^2) [6], [7], required 10 dB of dynamic range [10], and transmission through the phantom (≈10%), the sensitivity of the measurement system should be at least −17 dBm.

B. Reconstruction of APD Using PWS

The E-field can be propagated in space using the spectral-domain formulation defined by the PWS theory [26], [30]. This approach is widely used to retrieve SAR below 6 GHz [16], [31] as well as IPD [32], [33], [34] and APD [19] above 6 GHz. First, the Fourier transformation is applied to the measured electric field. This allows one to represent the spatial distribution of each field component over a transverse plane as a superposition of plane waves, referred as the PWS representation. In other words, the electromagnetic field on a transversal plane can be represented as an infinite sum of plane waves having different directions of propagation defined by couplet $\boldsymbol{K} = k_x\hat{x} + k_y\hat{y}$. The PWS of the E-field phasor component $\boldsymbol{E}(\boldsymbol{P}, z_0)$ over the plane $z = z_0$ and $\boldsymbol{P} = x\hat{x} + y\hat{y}$ is expressed as

$$\hat{\boldsymbol{E}}(\boldsymbol{K}, z_0) = \int_{\boldsymbol{R}} \boldsymbol{E}(\boldsymbol{P}, z_0) e^{j\boldsymbol{K}\boldsymbol{P}} d\boldsymbol{P}. \tag{1}$$

The PWS over any plane parallel to plane $z = z_0$ located at distance l in a homogeneous medium is computed by multiplying the PWS at $z = z_0$ by the propagator $e^{-jk_z l}$

$$\hat{\boldsymbol{E}}(\boldsymbol{K}, z_0 + l) = \hat{\boldsymbol{E}}(\boldsymbol{K}, z_0) e^{-jk_z l} \tag{2}$$

where k_z is the longitudinal propagation constant given as $k_z = (k^2 - |\boldsymbol{K}|^2)^{1/2}$, and k is the propagation constant.

The PWS is a convenient way to represent the propagation of the field in complex media (e.g., from the scanning plane $z = s + d_p$ to the surface of the phantom $z = 0$). $\hat{\boldsymbol{E}}_0^{||}(\boldsymbol{K})$, the PWS of $\boldsymbol{E}_0^{||}(\boldsymbol{K})$, is given as the superposition of the total E-field spectra propagating in the positive and negative directions along the z-axis and expressed as follows:

$$\hat{\boldsymbol{E}}_0^{||}(\boldsymbol{K}) = \hat{\boldsymbol{E}}_0^{||+}(\boldsymbol{K}) + \hat{\boldsymbol{E}}_0^{||-}(\boldsymbol{K}). \tag{3}$$

$\hat{\boldsymbol{E}}_0^{||+}$ and $\hat{\boldsymbol{E}}_0^{||-}$ are related to $\hat{\boldsymbol{E}}_p^{||}$ (the spectrum of $\boldsymbol{E}_p^{||}$) as follows (see Appendix):

$$\begin{aligned}\hat{\boldsymbol{E}}_0^{||+}(\boldsymbol{K}) = {} & \boldsymbol{T}_{ad}(\boldsymbol{I} - e^{-j2k_z^d s}\boldsymbol{R}_{da}^2)^{-1} \\ & \times \left(\boldsymbol{T}_{ad} e^{-k_z^d s}\boldsymbol{T}_{da}\left(\boldsymbol{I} - e^{-j2k_z^d s}\boldsymbol{R}_{da}^2\right)^{-1}\right)^{-1} \\ & \times \hat{\boldsymbol{E}}_p^{||}(\boldsymbol{K}) e^{jk_z^0 d_p}\end{aligned} \tag{4}$$

$$\begin{aligned}\hat{\boldsymbol{E}}_0^{||-}(\boldsymbol{K}) = {} & \boldsymbol{T}_{ad}(\boldsymbol{I} - e^{-j2k_z^d s}\boldsymbol{R}_{da}^2)^{-1} \\ & \times \left(\boldsymbol{T}_{ad} e^{-k_z^d s}\boldsymbol{T}_{da}\left(\boldsymbol{I} - e^{-j2k_z^d s}\boldsymbol{R}_{da}^2\right)^{-1}\right)^{-1} \\ & \times e^{-j2k_z^d s}\boldsymbol{R}_{da}\hat{\boldsymbol{E}}_p^{||}(\boldsymbol{K}) e^{jk_z^0 d_p}\end{aligned} \tag{5}$$

where $\boldsymbol{T}_{ad}$ and $\boldsymbol{T}_{da}$ are the spectral transmission coefficients at the air/dielectric and dielectric/air interfaces [26], respectively, $\boldsymbol{R}_{da}$ is the spectral reflection coefficient at the dielectric/air interface [26], $\boldsymbol{I}$ is the identity matrix, and k_z^d and k_z^0 are the longitudinal propagation constant of the dielectric and air, respectively. The spectral transmission and reflection operators, respectively, $\boldsymbol{T}$ and $\boldsymbol{R}$, for a dielectric interface between media 1 and 2 are defined as [12], [26]

$$\boldsymbol{T} = 2\boldsymbol{X}^{-1}(\boldsymbol{Y}_1 + \boldsymbol{Y}_2)^{-1}\boldsymbol{Y}_1\boldsymbol{X} \tag{6}$$

$$\boldsymbol{R} = \boldsymbol{X}^{-1}(\boldsymbol{Y}_1 + \boldsymbol{Y}_2)^{-1}(\boldsymbol{Y}_1 - \boldsymbol{Y}_2)\boldsymbol{X} \tag{7}$$

$$\boldsymbol{Y}_i = -\frac{1}{\omega\mu_0 k_{z,i}}\begin{bmatrix} k_i^2 - k_x^2 & -k_i k_y \\ -k_i k_y & k_i^2 - k_x^2 \end{bmatrix} \tag{8}$$

$$\boldsymbol{X} = \begin{bmatrix} 0 & 1 \\ -1 & 0 \end{bmatrix} \tag{9}$$

where $i \in [1, 2]$. $\boldsymbol{I}$ is given as follows:

$$\boldsymbol{I} = \begin{bmatrix} 1 & 0 \\ 0 & 1 \end{bmatrix}. \tag{10}$$

The normal field spectrum component is obtained from the tangential field spectra $\hat{\boldsymbol{E}}^{||}$ using the Gauss law

$$\hat{\boldsymbol{E}}_z^{+}(\boldsymbol{K}) = \frac{\boldsymbol{K}\cdot\hat{\boldsymbol{E}}^{||+}}{k_z}, \quad \hat{\boldsymbol{E}}_z^{-}(\boldsymbol{K}) = -\frac{\boldsymbol{K}\cdot\hat{\boldsymbol{E}}^{||-}}{k_z}. \tag{11}$$

The H-field spectrum is calculated as [30]

$$\hat{\boldsymbol{H}} = \left(-\frac{\boldsymbol{K}\times\hat{\boldsymbol{E}}^{+}}{\omega\mu}\right) - \left(-\frac{\boldsymbol{K}\times\hat{\boldsymbol{E}}^{-}}{\omega\mu}\right). \tag{12}$$

The spatial field components ($\boldsymbol{E}$ and $\boldsymbol{H}$) are retrieved using the inverse Fourier transform of the field spectra. The APD is calculated as

$$\text{APD} = \frac{1}{2}\text{Re}(\boldsymbol{E}\times\boldsymbol{H}^*)\cdot\hat{\boldsymbol{n}} \tag{13}$$

where $\hat{\boldsymbol{n}}$ is the unit vector normal to the APD evaluation surface.

Finally, the spatial peak APD (pAPD) is given as

$$p\text{APD} = \max(\text{APD}). \tag{14}$$

The peak spatial average APD (psAPD) equals to the maximum spatial average APD (sAPD) where sAPD is defined as the mean APD over a planar square shape area A [6]

$$ps\text{APD} = \max\left(\frac{1}{2A}\int\int_A \text{Re}(\boldsymbol{E}\times\boldsymbol{H}^*)\cdot\boldsymbol{ds}\right) \tag{15}$$

where A is the averaging square area equal to 1 or 4 cm^2 ($ps\text{APD}_{1\,\text{cm}^2}$ or $ps\text{APD}_{4\,\text{cm}^2}$, respectively), and $\boldsymbol{ds}$ is the integral variable vector normal to the averaging area A.

C. APD Reconstruction Accuracy

To assess the accuracy of the reconstruction technique, two types of simulations were performed using the time-domain solver of CST Microwave Studio 2022 using the finite integration technique (FIT). The total number of mesh cells reaches about 13 and 21 million for the reference horn and dipole array antennas, respectively (in the presence of the phantom). The smallest mesh cell dimension is 316 μm ($\approx\lambda_0/15$) in

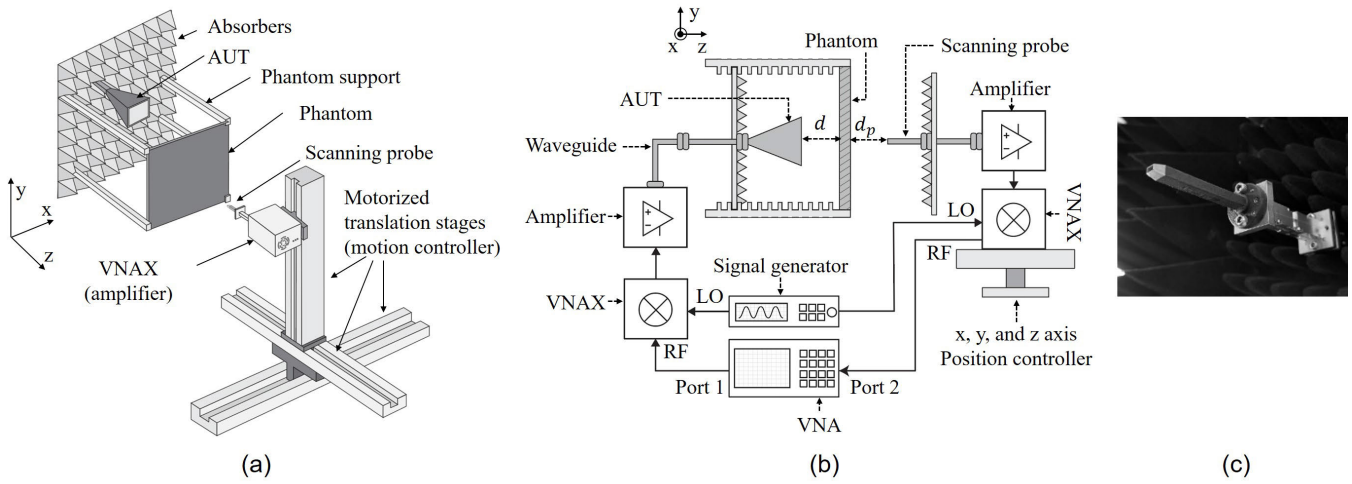

Fig. 3. Measurement setup. (a) Three-dimensional outline. (b) Full-chain measurement system. (c) OWG field probe (dimensions are in mm).

free-space and 92 μm inside the phantom ($\approx\lambda_d/15$). Open boundaries [perfectly matched layers (PMLs)] were used. In simulations, the antenna input power is set to 10 mW.

In one simulation, the E-field monitor is set to compute the E-field vector in free-space (without OWG probe) at the opposite side of the phantom with respect to the AUT ($z = s + d_p$) ($E_{(p,s)}$). $E_{(p,s)}$ is used to reconstruct APD at the surface of the phantom ($\text{APD}_{(r,s)}$). In another simulation, a half-space skin-equivalent phantom is used to compute the APD at its surface using the power monitor ($\text{APD}_{(s)}$) ($\epsilon_r = 7.98 - j11.90$). The relative error of the reconstruction technique is assessed as follows:

$$\Delta_i^s = \left| \frac{\text{APD}_{(r,s)}}{\text{APD}_{(s)}} - 1 \right| \tag{16}$$

where Δ_i denotes the relative error for $p\text{APD}$, $ps\text{APD}_{1\,\text{cm}^2}$, or $ps\text{APD}_{4\,\text{cm}^2}$ (Δ_{peak}, $\Delta_{1\,\text{cm}^2}$, and $\Delta_{4\,\text{cm}^2}$, respectively).

III. Measurement System

A. Near-Field Scanner

The measurement system is schematically represented in Fig. 3(a) and (b). VNA (Agilent N5242A) operating at 10 MHz–26.5 GHz is used to generate a radio frequency (RF) signal. The frequency is upconverted to the 50–75-GHz band using a VNA extender (VNAX) (Vadiodes WR15). The local oscillator (LO) of the VNAX is controlled using a microwave analog signal generator (Keysight N5173B). The output signal from the VNAX is amplified and used to feed the AUT through a set of WR15 waveguides. The phantom is set at a distance d from the AUT. The amplitude and phase of the transmitted through the phantom E-field are measured using a linearly polarized tapered OWG [Fig. 3(c)]. The use of amplifiers at the emission and reception stages results in measurement sensitivity better than -60 dBm. The amplitude and phase of the E-field are derived from the amplitude and phase difference between the two ports of the VNA.

A position controller (Newport XPS) holding the measurement probe is used to scan the field over a planar surface. The dimensions of the scanning surface are 40×40 mm ($8 \times 8\ \lambda_0$) covering -30 dB area with respect to the peak E-field in the scanning plane. This results in a typical measurement duration of 2 h 40 min. It can be significantly reduced using IR-based measurement (≈few minutes) [23], [24]. The measured signal is amplified, downconverted by a VNAX transceiver, and transmitted to the second port of the VNA. Switching from the measurement of the main-polarization (y-axis) component to the cross-polarization (x-axis) component of the E-field vector ($\boldsymbol{E}^{||}_{(p,m)}$) is performed using a 90° mechanical rotation of the AUT.

Measured by VNA, the relative amplitude and phase are converted into absolute APD using a probe calibration method recommended in [10]. In brief, the method consists in calibrating the measurement probe in a known field radiated by a reference antenna ($\hat{\boldsymbol{E}}_{(\text{ref},s)}$). As reference antenna, we used a V-band linearly polarized conical horn with 21.4-dB gain (QuinStar, CA, USA). The field is computed outside the reactive field region at $d = 10 \cdot \lambda_0$ to avoid the influence of the probe on the reference antenna. Then the field is measured at the same location ($d = 10 \cdot \lambda_0$) using the near-field scanner ($\hat{\boldsymbol{E}}_{(\text{ref},m)}$). A probe correction matrix is calculated as

$$\boldsymbol{M}_c = \frac{\hat{\boldsymbol{E}}_{(\text{ref},m)}}{\hat{\boldsymbol{E}}_{(\text{ref},s)}}. \tag{17}$$

The absolute values of E-field ($\hat{\boldsymbol{E}}_{(p,m)}$) are retrieved from the relative E-field measured by VNA ($\hat{\boldsymbol{E}}_{(p,r,m)}$) as follows:

$$\hat{\boldsymbol{E}}_{(p,m)} = \boldsymbol{M}_c \cdot \hat{\boldsymbol{E}}_{(p,r,m)}. \tag{18}$$

B. E-Field Probe Effect

The impact of the reflection and standing wave between the probe and phantom on APD was investigated numerically considering two different scenarios. In the first scenario, APD was computed using full-wave simulation accounting for the phantom/probe interaction. In the second scenario, the AUT and phantom were replaced by their equivalent source and used to compute APD. The equivalent source reproduces the radiation of AUT with discrepancy lower than 1% in terms of E-field intensity and power density. The scattered from

TABLE I

Δ_i^j (%)

			Dipole Array			Slotted horn		
			Δ^j_{peak}	$\Delta^j_{1cm^2}$	$\Delta^j_{4cm^2}$	Δ^j_{peak}	$\Delta^j_{1cm^2}$	$\Delta^j_{4cm^2}$
Numerical								
Δ_i^s	max $(d \in [2-10]$ mm)		4	3.2	2.9	4.3	2.4	2
	d (mm)	2	1.4	1.5	1.7	4.3	0.3	0.1
		5	0.2	2.2	1.4	2	0.7	0.2
		10	2	2.8	2.6	1.5	0.3	0.6
Experimental								
Δ_i^m	d (mm)	2	8.9	1.9	2.5	4.4	10.5	15.7
		5	5.5	11.4	12.5	6	2.9	2.2
		10	9.2	14.9	1	13.2	9.5	6.6

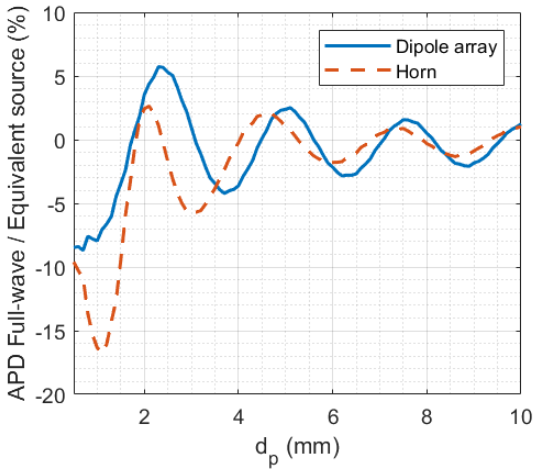

Fig. 4. Effect of the phantom/probe interaction on APD.

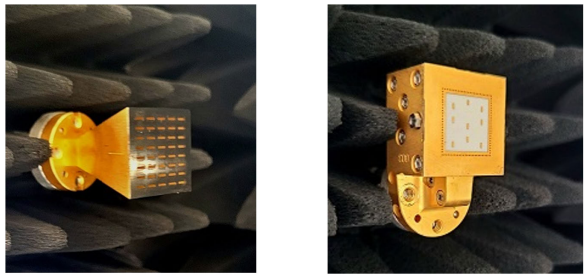

Fig. 5. Reference antennas used as AUT. (a) Pyramidal horn with slot array and (b) cavity-fed dipole array [10].

the probe field is reflected back by the phantom in the first scenario, whereas it is neglected in the second scenario. The ratio between APD computed using full-wave and equivalent source is given in Fig. 4. This result suggests that the probe should be located far enough from the phantom (for $d_p \geq$ 2.5 mm, the changes in APD are $<\pm 6\%$). Nevertheless, d_p should be kept sufficiently short to minimize the numerical error related to E-field free-space back propagation from $z = s + d_p$ to $z = s$ plane, which increases with d_p. The best tradeoff is found for $2.5 \leq d_p < 5$ mm where the maximum error on APD reconstruction due to the standing wave and back propagation is within $\pm 6\%$. Measurements of the dipole array and horn antennas are performed for d_p equal to 2.5 mm.

IV. Validation for Reference Antennas

The proposed technique was validated for two reference antennas (pyramidal horn and dipole array antennas) defined by IEC/IEEE 63195 standard for validation of the power density measurement systems (Fig. 5).

A. APD Distribution

The spatial distributions of $\text{APD}_{(s)}$, $\text{APD}_{(r,s)}$, and $\text{APD}_{(r,m)}$ are presented in Figs. 6 and 7 for $d = 2$, 5, and 10 mm. They are compared using the correlation coefficient Υ defined as

$$\Upsilon = \frac{\sum_m \sum_n (X_{mn} - \bar{X})(Y_{mn} - \bar{Y})}{\sqrt{\sum_m \sum_n (X_{mn} - \bar{X})^2 \sum_m \sum_n (Y_{mn} - \bar{Y})^2}} \quad (19)$$

where X and Y are the distributions to compare, and $\bar{X}$ and $\bar{Y}$ are, respectively, the mean values of X and Y. The parameter Υ is an indicator of how close the two relative distributions fit. The results demonstrate 99.9% fit between the simulated $\text{APD}_{(r,s)}$ and $\text{APD}_{(s)}$ patterns and around 95% ($\pm 1\%$) between the measured $\text{APD}_{(r,m)}$ and the simulated $\text{APD}_{(s)}$ for both the antennas.

As seen in Figs. 6 and 7, the main beam shape and position are well-reproduced for both the reference antennas and all the distances. The decrease in APD reconstruction accuracy for side lobes is mainly attributed to the directional effect of the probe. Advanced probe compensation schemes to improve the side lobes' measurements are out of the scope of this study and constitute one of its perspectives. For the horn antenna, discrepancies of about 3 dB between $\text{APD}_{(r,m)}$ and $\text{APD}_{(s)}$ distributions are noted in the $-1 < x < 1$ mm interval (Fig. 6(c)—1-D distribution). They are attributed to the averaging effect of the probe, which integrates the field over the surface of its aperture (1.88 × 3.86 mm).

B. Spatial-Average APD

$\text{APD}_{(s)}$, $\text{APD}_{(r,s)}$, and $\text{APD}_{(r,m)}$ profiles as a function of d are shown in Fig. 8. The relative error of the $\text{APD}_{(r,m)}$ reconstruction from the measured data is calculated as

$$\Delta_i^m = \left| \frac{\text{APD}_{(r,m)}}{\text{APD}_{(s)}} - 1 \right|. \quad (20)$$

Δ_i^s and Δ_i^m are given in Table I.

The results show an excellent agreement between $\text{APD}_{(s)}$ and $\text{APD}_{(r,s)}$, peak and averaged over 1 and 4 cm^2. The

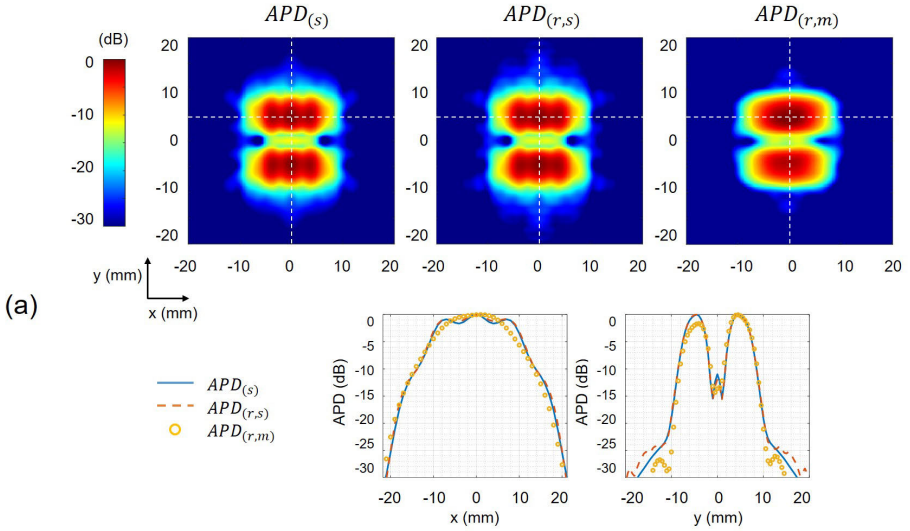

1D profiles along the lines (dashed white) parallel to x and y axis intersecting the peak APD

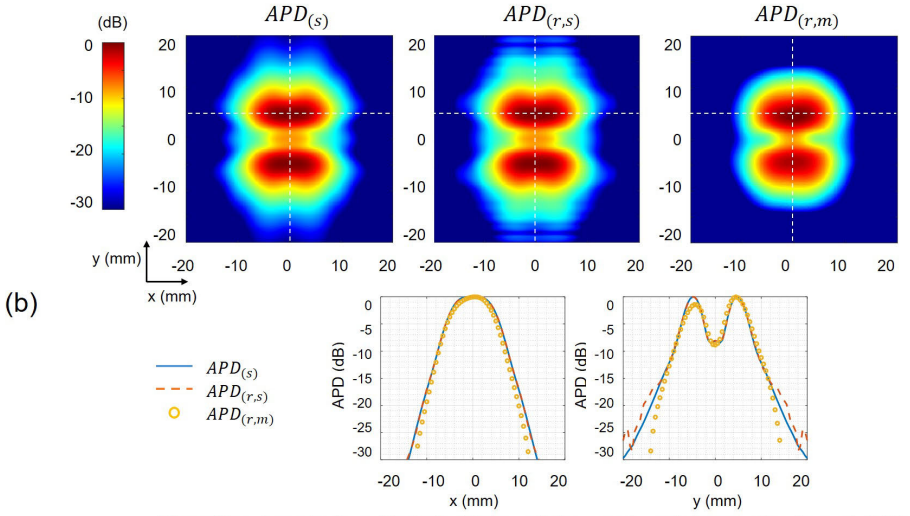

1D profiles along the lines (dashed white) parallel to x and y axis intersecting the peak APD

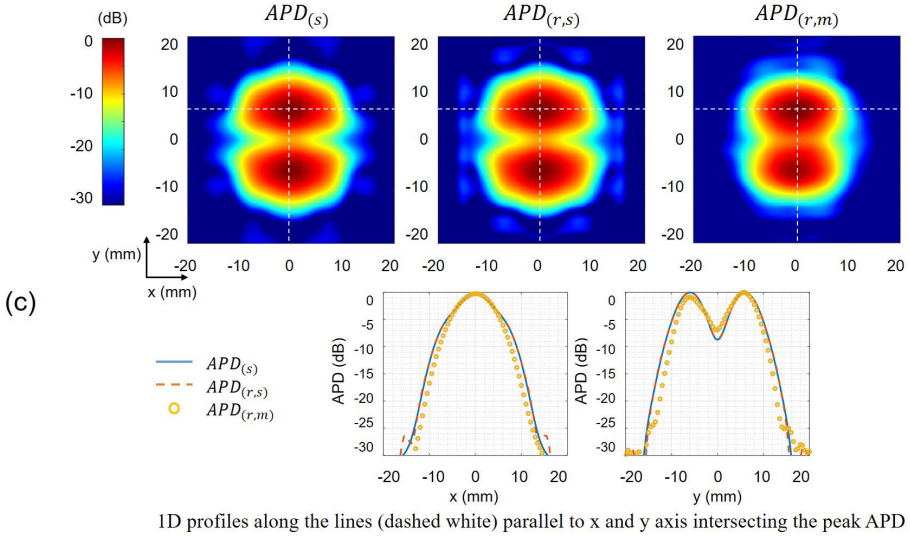

1D profiles along the lines (dashed white) parallel to x and y axis intersecting the peak APD

Fig. 6. APD distribution for the horn antenna at (a) $d = 2$ mm, (b) $d = 5$ mm, and (c) $d = 10$ mm.

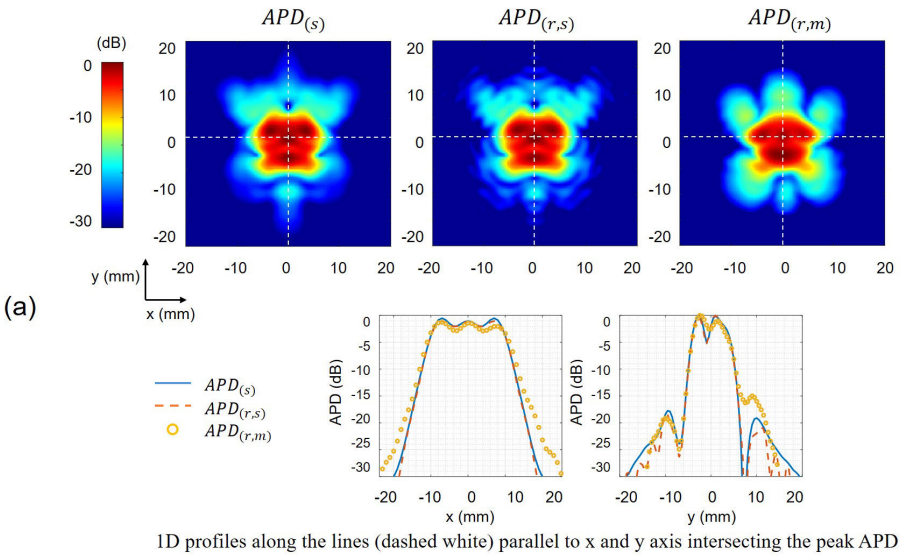

1D profiles along the lines (dashed white) parallel to x and y axis intersecting the peak APD

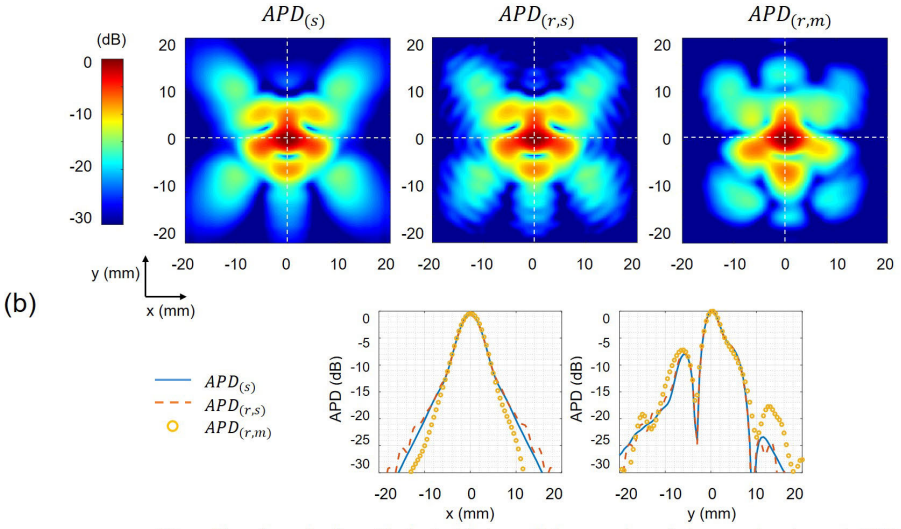

1D profiles along the lines (dashed white) parallel to x and y axis intersecting the peak APD

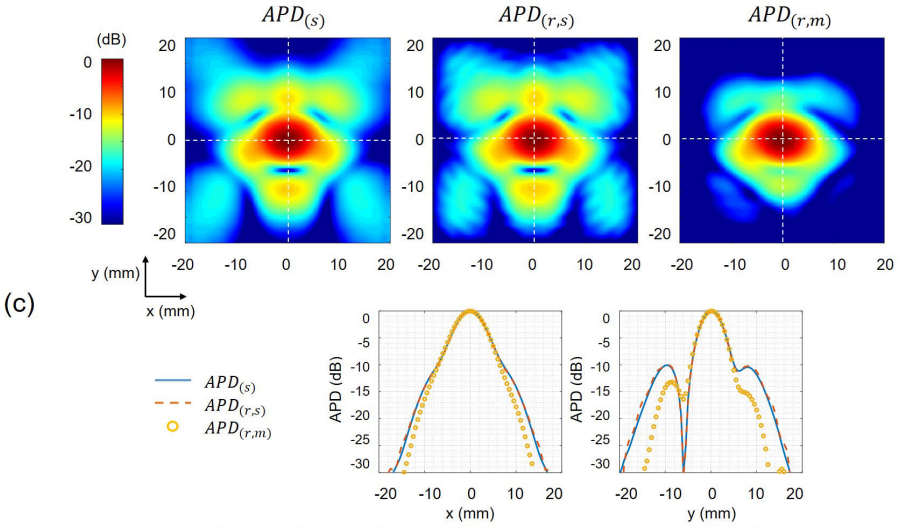

1D profiles along the lines (dashed white) parallel to x and y axis intersecting the peak APD

Fig. 7. APD distribution for the dipole array antenna at (a) $d = 2$ mm, (b) $d = 5$ mm, and (c) $d = 10$ mm.

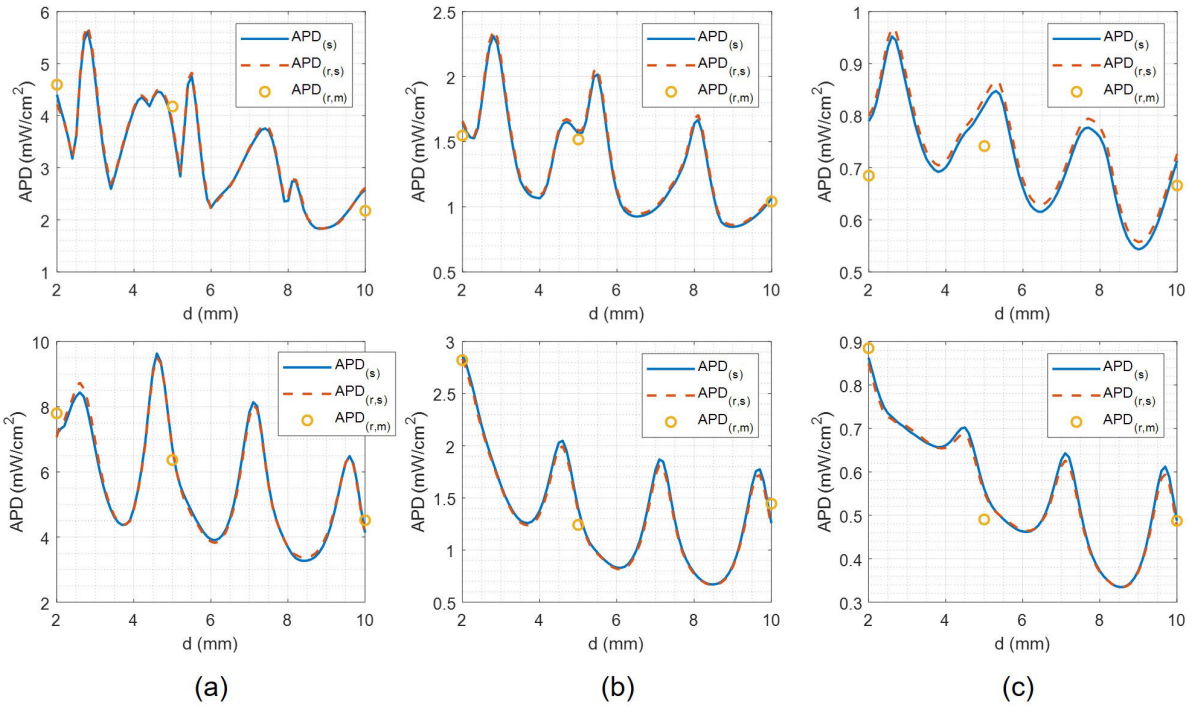

Fig. 8. APD for horn (top) and dipole array (bottom) antennas. (a) pAPD. (b) $ps\text{APD}_{1\,\text{cm}^2}$. (c) $ps\text{APD}_{4\,\text{cm}^2}$.

maximum Δ^s_{peak} of 4.3% (0.18 dB) is found for the horn antenna at $d = 2$ mm. The maximum $\Delta^s_{1\,\text{cm}^2}$ and $\Delta^s_{4\,\text{cm}^2}$ equal to 3.2% (0.14 dB) and 2.9% (0.13 dB), respectively, were found for the dipole array at $d = 6.6$ and 3.1 mm, respectively. These errors are lower at $d = 2$, 5, and 10 mm.

A very good agreement is also demonstrated between simulations and measurements ($\text{APD}_{(s)}$ and $\text{APD}_{(r,m)}$). The maximum Δ^m_{peak}, $\Delta^m_{1\,\text{cm}^2}$, and $\Delta^m_{4\,\text{cm}^2}$ are equal to 9.2% (0.38 dB), 14.9% (0.6 dB), and 12.5% (0.51 dB), respectively, for the dipole array antenna. For the horn antenna, the maximum Δ^m_{peak}, $\Delta^m_{1\,\text{cm}^2}$, and $\Delta^m_{4\,\text{cm}^2}$ are equal to 13.2% (0.54 dB), 10.5% (0.43 dB), and 15.7% (0.63 dB), respectively. In some cases (e.g., dipole array at $d = 5$ mm), the error on the averaged $\text{APD}_{(r,m)}$ exceeds the error on its peak ($\Delta^m_{\text{peak}} < \Delta^m_{1\,\text{cm}^2}$ and $\Delta^m_{\text{peak}} < \Delta^m_{4\,\text{cm}^2}$) [Fig. 7(b)]. This is attributed to the directional effect of the OWG probe, which introduces errors in the E-field distribution.

Note that APD strongly changes with d. For example, the horn antenna position shift from $d = 2.8$ to 3.4 mm results in 116% (3.34 dB), 76% (2.46 dB), and 32% (1.21 dB) decrease in pAPD, $ps\text{APD}_{1\,\text{cm}^2}$, and $ps\text{APD}_{4\,\text{cm}^2}$, respectively. Therefore, determination of the maximum APD would require measurements with a fine spatial sampling resolution (of the order of hundreds of μm).

C. Uncertainty Analysis

The main sources of uncertainty for the proposed method are listed hereafter.

1) Calibration
   a) *Amplifier Linearity:* ±2% (0.09 dB).
   b) *Complex Permittivity (Due to Errors in Permittivity Characterization):* ±5% (±0.21 dB) for the real part and ±10% (±0.41 dB) for the imaginary part.
   c) *Probe Positioning:* ±3% (±0.13 dB).
   d) *Probe Calibration:* ±6% (0.25 dB), ±13.5% (0.55 dB), and ±5.4% (0.23 dB) on peak $\boldsymbol{E}_p$, spatial average of $\|\boldsymbol{E}_p\|$ over 1 and 4 cm^2, respectively.
2) Scanning probe
   a) *Position Along z-Axis:* ±100 μm.
   b) *Position Along x-Axis and y-Axis:* ±50 μm.
   c) *Amplitude and Phase:* ±5% (±0.21 dB).
   d) *Phantom/Probe Interaction:* ±5.4% (±0.23 dB).
   e) *AUT/Probe Interaction:* ±1% (±0.04 dB).
3) Phantom
   a) *Complex Permittivity (Due to Fabrication Errors):* ±2.9% (±0.12 dB) for the real part and ±6% (±0.25 dB) for the imaginary part.
   b) *Thickness:* ±50 μm.
   c) *APD in Skin:* Differences between APD (pAPD, $ps\text{APD}_{1\,\text{cm}^2}$, and $ps\text{APD}_{4\,\text{cm}^2}$) at the surface of the skin [27] and the fabricated phantom are within ±4.95% (±0.21 dB).
4) Postprocessing
   a) *APD Reconstruction:* ±4% (±0.17 dB).
   b) *Scanning Area Truncation:* Truncation error is negligibly small for the scanning area ($8 \times 8\lambda_0$).
   c) *Sampling:* ±1% (±0.04 dB).
5) Device under test (DUT)
   a) *Positioning:* ±3% (±0.13 dB).
   b) *Power Drift:* ±5% (±0.21 dB).

The uncertainty budget is provided in Table II. We used the uncertainty analysis methodology from [10]. Uncertainties reported in Table II correspond to the maximum error in APD (pAPD, $ps\text{APD}_{1\,\text{cm}^2}$, and $ps\text{APD}_{4\,\text{cm}^2}$) produced by

TABLE II
APD UNCERTAINTY BUDGET

Source of errors				Dipole Array			Slotted horn		
				pAPD	psAPD		pAPD	psAPD	
					$1cm^2$	$4cm^2$		$1cm^2$	$4cm^2$
Calibration	1.1	Complex permitivity	Real	0.09	0.09	0.09	0.05	0.05	0.05
			Imag	0.19	0.21	0.22	0.11	0.12	0.13
	1.2	Probe positioning		0.13	0.09	0.1	0.08	0.05	0.06
	1.3	Amplifier linearity		0.09	0.09	0.09	0.05	0.05	0.05
	1.4	Probe calibration		0.25	0.55	0.23	0.14	0.32	0.13
Scanning probe	2.1	Position (z-axis)		0.13	0.09	0.1	0.08	0.05	0.06
	2.2	Position (x- and y-axis)		0.28	0.28	0.61	0.16	0.16	0.35
	2.3	Amplitude and phase		0.37	0.37	0.37	0.21	0.21	0.21
	2.4	Phantom/probe interaction		0.49	0.49	0.49	0.28	0.28	0.28
	2.5	Interaction with AUT		0.09	0.09	0.09	0.05	0.05	0.05
Phantom	3.1	Complex permitivity	Real	0.12	0.13	0.13	0.07	0.08	0.08
			Imag	0.25	0.26	0.27	0.14	0.15	0.16
	3.2	Thickness		0.06	0.06	0.06	0.04	0.04	0.04
	3.3	APD in phantom vs. skin		0.21	0.21	0.21	0.12	0.12	0.12
Post-processing	4.1	Reconstruction method		0.17	0.17	0.17	0.1	0.1	0.1
	4.2	Scanning area truncation		0	0	0	0	0	0
	4.3	Sampling		0.04	0.01	0.01	0.02	0.01	0.01
DUT	5.1	Positioning		0.13	0.09	0.1	0.08	0.05	0.06
	5.2	Power drift		0.21	0.21	0.21	0.12	0.12	0.12
Combined uncertainty							0.57	0.64	0.65
Expanded uncertainty ($k = 2$)							1.14	1.27	1.3

the corresponding source of error. The uncertainties listed in Table II are assumed to have a rectangular probability distribution, and hence, the standard uncertainty is obtained as the ratio of the uncertainty over the divisor $\sqrt{3}$ [10], [35]. The weighting factor is set to $c_i = 1$ and the degrees of freedom to $v_i = \infty$. The combined and expanded uncertainties (with the coverage factor $k = 2$) on APD (pAPD, $ps\text{APD}_{1\,\text{cm}^2}$, and $ps\text{APD}_{4\,\text{cm}^2}$) are assessed according to the guidelines in ISO/IEC Guide 98-3 [33] and found to be below 16% (0.65 dB) and 35% (1.3 dB), respectively.

Uncertainties related to phantom/probe coupling and probe calibration represent the main sources of error. Reducing uncertainties related to these two sources of error would allow to reduce the overall uncertainty. This constitutes one of the perspectives of this study.

D. Free-Space Versus In-Liquid Measurements

The conventional dosimetry methods developed for SAR measurements use liquid tissue-equivalent phantoms [31]. Due to increasing with frequency losses in tissue-simulating liquids, free-space measurements ensure enhanced robustness with respect to probe positioning compared with the in-liquid measurements. Indeed, as shown in Table II, in free-space the uncertainty related to the probe positioning along the z-axis results in pAPD, $ps\text{APD}_{1\,\text{cm}^2}$, and $ps\text{APD}_{4\,\text{cm}^2}$ uncertainties of 2.9% (0.13 dB), 2.1% (0.09 dB), and 2.3% (0.1 dB), respectively. Assuming that the measurements are performed not in free-space but in a liquid with the permittivity of skin ($\epsilon_r = 7.98 - 10.98j$), the same positioning tolerance of the probe (i.e., ± 100 μm) would result in pAPD, $ps\text{APD}_{1\,\text{cm}^2}$, and $ps\text{APD}_{4\,\text{cm}^2}$ uncertainties of 34.7% (1.85 dB), 34.4% (1.83 dB), 34.4% (1.83 dB), respectively. The overall expended uncertainty for $ps\text{APD}_{4\,\text{cm}^2}$ would increase from 35% (1.3 dB) to 77% (2.48 dB). This uncertainty rise is due to the sharp E-field gradient in the lossy liquid phantoms at mmWaves. This suggests that performing measurements in free-space, using a thin reflectivity-based phantom, reduces the measurement uncertainty compared with in-liquid measurements (assuming all other parameters of the measurement system remain the same).

V. CONCLUSION

In this article, we introduced a novel method for APD assessment, based on free-space E-field measurements, accounting for the effect of the body presence. The system uses a reflectivity-based solid phantom that mimics the skin scattering characteristics at one side (AUT side) while providing an enhanced transmission through the phantom to maximize the E-field magnitude at the opposite side. A tapered open-ended waveguide is used to measure the E-field transmitted through the phantom. The method was validated using the reference cavity-fed dipole array and slotted pyramidal horn antennas at 60 GHz.

An excellent agreement was found between the simulated APD (peak, averaged, and distribution) and the reconstructed one from the simulated E-field. The maximum relative error on the reconstructed pAPD, $ps\text{APD}_{1\,\text{cm}^2}$, and $ps\text{APD}_{4\,\text{cm}^2}$ from the simulated tangential components of the E-field was found to be 4.3% (0.18 dB) ($d = 2$ mm for horn), 3.2% (0.14 dB) ($d = 6.6$ mm for dipole array), and 2.9% (0.13 dB) ($d = 3.1$ mm for dipole array), respectively. The correlation between the simulated and numerically reconstructed APDs was found to be higher than 99.9%.

A very good agreement was found between the simulated APD and the one reconstructed from measurements as well. The maximum errors on pAPD, $ps\text{APD}_{1\,\text{cm}^2}$, and $ps\text{APD}_{4\,\text{cm}^2}$ for all the phantom-to-probe separation distances d of 2, 5, and 10 mm do not exceed 15.7% (0.63 dB).

The uncertainty budget analysis for the proposed APD measurement method was performed according to IEC/IEEE

63195. The expanded uncertainty in pAPD, $ps\text{APD}_{1\,\text{cm}^2}$, and $ps\text{APD}_{4\,\text{cm}^2}$ is 1.14, 1.27, and 1.3 dB, respectively.

This proof-of-concept study demonstrates a strong potential of this new technique for APD assessment and compliance testing of mmWave wireless devices. Scaling the proposed APD approach to other FR2 bands constitutes a perspective of this study.

APPENDIX
APD RECONSTRUCTION FROM FREE-SPACE E-FIELD BACKPROPAGATION

A part of the incident field spectrum ($\hat{\boldsymbol{E}}^{||}_{\text{inc}}$) is transmitted to the phantom. The transmitted field propagates from plane $z = 0$ to $z = s$ where a part of it is transmitted to the air ($z > s$) and the other part is reflected. The latter propagates toward $z = 0$ in the reverse direction of the z-axis where it is reflected back toward $z = s$. This forth and backpropagation keeps going until the amplitude of the field inside the phantom vanishes after n iterations. ($\hat{\boldsymbol{E}}^{||}_{p}$) is given as the superposition of the total transmitted field at $z > s$ as

$$\hat{\boldsymbol{E}}^{||}_{p}(\boldsymbol{K}) = \hat{\boldsymbol{E}}^{||}_{\text{inc}}(\boldsymbol{K})\boldsymbol{T}_{ad}e^{-jk^d_z s}\boldsymbol{T}_{da} \times \left(\boldsymbol{I}+\boldsymbol{R}^2_{da}e^{-j2k^d_z s}+\cdots+\left(\boldsymbol{I}+\boldsymbol{R}^2_{da}e^{-j2k^d_z s}\right)^n\right)e^{-jk^0_z d_p}. \tag{21}$$

Equation (19) is a geometric series, also called the Neumann series [36], with the common ratio $\boldsymbol{R}^2_{da}e^{-j2k^d_z s}$. If the eigenvalue of $\boldsymbol{R}^2_{da}e^{-j2k^d_z s}$ is within ± 1, the geometric series converges to the following as n tends to infinity:

$$\hat{\boldsymbol{E}}^{||}_{p}(\boldsymbol{K}) = \boldsymbol{T}_{ad}e^{-jk^d_z s}\boldsymbol{T}_{da}\left(\boldsymbol{I}-\boldsymbol{R}^2_{da}e^{-j2k^d_z s}\right)^{-1}e^{-jk^d_0 d_p}\hat{\boldsymbol{E}}^{||}_{\text{inc}}(\boldsymbol{K}). \tag{22}$$

The field inside the phantom can be expressed as the superposition of the total E-field spectra propagating in the positive and negative directions along the z-axis. $\hat{\boldsymbol{E}}^{||}_{a}$, given as the superposition of $\hat{\boldsymbol{E}}^{||+}_{a}$ and $\hat{\boldsymbol{E}}^{||-}_{a}$, is expressed using $\hat{\boldsymbol{E}}^{||}_{\text{inc}}$ as follows:

$$\hat{\boldsymbol{E}}^{||}_{a}(\boldsymbol{K}) = \boldsymbol{T}_{ad}(\boldsymbol{I}+\boldsymbol{R}_{da}e^{-j2k^d_z s})\left(\boldsymbol{I}-\boldsymbol{R}^2_{da}e^{-j2k^d_z s}\right)^{-1}\hat{\boldsymbol{E}}^{||}_{\text{inc}}(\boldsymbol{K}) \tag{23}$$

where

$$\hat{\boldsymbol{E}}^{||+}_{a}(\boldsymbol{K}) = \boldsymbol{T}_{ad}\left(\boldsymbol{I}-\boldsymbol{R}^2_{da}e^{-j2k^d_z s}\right)^{-1}\hat{\boldsymbol{E}}^{||}_{\text{inc}}(\boldsymbol{K}) \tag{24}$$

and

$$\hat{\boldsymbol{E}}^{||-}_{a}(\boldsymbol{K}) = \boldsymbol{T}_{ad}\boldsymbol{R}_{da}e^{-j2k^d_z s}\left(\boldsymbol{I}-\boldsymbol{R}^2_{da}e^{-j2k^d_z s}\right)^{-1}\hat{\boldsymbol{E}}^{||}_{\text{inc}}(\boldsymbol{K}). \tag{25}$$

From (20), $\hat{\boldsymbol{E}}^{||}_{\text{inc}}$ is expressed using $\hat{\boldsymbol{E}}^{||}_{p}$ as follows:

$$\hat{\boldsymbol{E}}^{||}_{\text{inc}}(\boldsymbol{K}) = \left(\boldsymbol{T}_{ad}e^{-jk^d_z s}\boldsymbol{T}_{da}\left(\boldsymbol{I}-\boldsymbol{R}^2_{da}e^{-j2k^d_z s}\right)^{-1}\right)^{-1}e^{jk^d_0 d_p}\hat{\boldsymbol{E}}^{||}_{p}(\boldsymbol{K}). \tag{26}$$

Replacing $\hat{\boldsymbol{E}}^{||}_{\text{inc}}$ in (21)

$$\hat{\boldsymbol{E}}^{||}_{a}(\boldsymbol{K}) = \boldsymbol{T}_{ad}(\boldsymbol{I}+\boldsymbol{R}_{da}e^{-j2k^d_z s})(\boldsymbol{I}-\boldsymbol{R}^2_{da}e^{-j2k^d_z s})^{-1} \times \left(\boldsymbol{T}_{ad}e^{-jk^d_z s}\boldsymbol{T}_{da}\left(\boldsymbol{I}-\boldsymbol{R}^2_{da}e^{-j2k^d_z s}\right)^{-1}\right)^{-1} \times e^{jk^d_0 d_p}\hat{\boldsymbol{E}}^{||}_{p}(\boldsymbol{K}) \tag{27}$$

with

$$\hat{\boldsymbol{E}}^{||+}_{a}(\boldsymbol{K}) = \boldsymbol{T}_{ad}\left(\boldsymbol{I}-\boldsymbol{R}^2_{da}e^{-j2k^d_z s}\right)^{-1} \times \left(\boldsymbol{T}_{ad}e^{-jk^d_z s}\boldsymbol{T}_{da}\left(\boldsymbol{I}-\boldsymbol{R}^2_{da}e^{-j2k^d_z s}\right)^{-1}\right)^{-1} \times e^{jk^d_0 d_p}\hat{\boldsymbol{E}}^{||}_{p}(\boldsymbol{K}) \tag{28}$$

and

$$\hat{\boldsymbol{E}}^{||-}_{a}(\boldsymbol{K}) = \boldsymbol{T}_{ad}\boldsymbol{R}_{da}e^{-j2k^d_z s}\left(\boldsymbol{I}-\boldsymbol{R}^2_{da}e^{-j2k^d_z s}\right)^{-1} \times \left(\boldsymbol{T}_{ad}e^{-jk^d_z s}\boldsymbol{T}_{da}\left(\boldsymbol{I}-\boldsymbol{R}^2_{da}e^{-j2k^d_z s}\right)^{-1}\right)^{-1} \times e^{jk^d_0 d_p}\hat{\boldsymbol{E}}^{||}_{p}(\boldsymbol{K}). \tag{29}$$

ACKNOWLEDGMENT

The authors would like to thank F. Boutet for the kind assistance in using the quasi-optical setup for complex permittivity measurements. They also acknowledge the Mobile & Wireless Forum (MWF) for providing the reference antennas.

REFERENCES

[1] HUAWEI. (2017). *5G Spectrum Public Policy Position*. [Online]. Available: https://www-file.huawei.com/-/media/CORPORATE/PDF

[2] GSMA. (Jun. 2022). *5G Spectrum GSMA Public Policy Position*. [Online]. Available: https://www.gsma.com/spectrum/wp-content/uploads/2022/06/5G-Spectrum-Positions.pdf

[3] C. Dehos, J. L. González, A. D. Domenico, D. Kténas, and L. Dussopt, "Millimeter-wave access and backhauling: The solution to the exponential data traffic increase in 5G mobile communications cystems," *IEEE Commun. Mag.*, vol. 52, no. 9, p. 8895, Sep. 2014.

[4] MiWaves Project FP7 CORDIS European Commission. *Beyond 2020 Heterogeneous Wireless Network With Nillimeter Wave Small Cell Access and Backhauling*. Accessed: Oct. 10, 2022. [Online]. Available: https://cordis.europa.eu/project/id/619563/fr

[5] T. Baykas et al., "IEEE 802.15.3c: The first IEEE wireless standard for data rates over 1 Gb/s," *IEEE Commun. Mag.*, vol. 49, no. 7, pp. 114–121, Jul. 2011.

[6] International Commission on Non-Ionizing Radiation Protection (ICNIRP), "Guideliens for limiting exposure to electromagnetic fields (100 kHz to 300 GHz)," *Health Phys.*, vol. 118, no. 5, pp. 483–524, May 2020.

[7] *safety Levels With Respect to Human Exposure to Electric, Magnetic, and Electromagnetic Fields, 0 Hz to 300 GHz*, IEEE Standard C95.1, Aug. 2020.

[8] K. Li et al., "Calculated epithelial/absorbed power density for exposure from antennas at 10–90 GHz: Intercomparison study using a planar skin model," *IEEE Access*, vol. 11, pp. 7420–7435, 2023.

[9] A. L. Kapetanovic, G. Sacco, D. Poljak, and M. Zhadobov, "Area-averaged transmitted and absorbed power density on a realistic ear model," *IEEE J. Electromagn., RF Microw. Med. Biol.*, vol. 7, no. 1, pp. 39–45, Mar. 2023.

[10] *Assessment of Power Density of Human Exposure to Radio Frequency Fields from Wireless Devices in Close Proximity to the Head and Body (Frequency Range of 6 GHz to 300 GHz)*, Standard IEC/IEEE 63195-2, May 2022.

[11] S. Pfeifer et al., "Total field reconstruction in the near field using pseudo-vector E-field measurements," *IEEE Trans. Electromagn. Compat.*, vol. 61, no. 2, pp. 476–486, Apr. 2019.

[12] G. Hislop, G. C. James, and A. Hellicar, "Phase retrieval of scattered fields," *IEEE Trans. Antennas Propag.*, vol. 55, no. 8, pp. 2332–2341, Aug. 2007.
[13] M. Ziane, R. Sauleau, and M. Zhadobov, "Antenna/body coupling in the near-field at 60 GHz: Impact on the absorbed power density," *Appl. Sci.*, vol. 10, no. 21, p. 7392, Oct. 2020.
[14] B. Derat, A. Cozza, and J.-C. Bolomey, "Influence of source-phantom multiple interactions on the field transmitted in a flat phantom," in *Proc. 18th Int. Zurich Symp. Electromagn. Compat.*, Munich, Germany, Sep. 2007, Art. no. 139142.
[15] A. Cozza, B. Derat, and S. Pannetrat. *System for Measuring an Electromagnetic Field*. Accessed: Oct. 10, 2022. [Online]. Available: https://emc.live/wp-content/uploads/2017/01/002-2013-iWAT-Publication-ART-MAN-technology.pdf
[16] B. Derat, L. Aberbour, and A. Cozza, "Near-field and vector signal analysis techniques applied to specific absorption rate measurement," in *IEEE MTT-S Int. Microw. Symp. Dig.*, Taiwan, Sep. 2015, pp. 34–35.
[17] SPEAG. *DASY 8 SAR Measurement*. Accessed: Oct. 10, 2022. [Online]. Available: https://speag.swiss/products/dasy8/overview/?pdf=view
[18] MVG. *ComoSAR SAR Measurement System*. Accessed: Oct. 10, 2022. [Online]. Available: https://www.mvg-world.com/fr/produits/sar/sar-systems/comosar-v5
[19] S. F. Jafari, R. Sarraf Shirazi, G. Moradi, A. Sibille, and J. Wiart, "Absorbed/epithelial power density assessment using plane-wave spectrum method from inside the skin tissue above 6 GHz," *IEEE Trans. Instrum. Meas.*, vol. 71, pp. 1–8, 2022.
[20] F. Karimi et al., "Method and implementations to measure the absorbed power density," in *IEEE MTT-S Int. Microw. Symp. Dig.*, Suzhou, China, May 2022, pp. 129–131.
[21] SPEAG. *DASY 8 APD Module (10–45 GHz)*. Accessed: Oct. 10, 2022. [Online]. Available: https://speag.swiss/products/dasy8/m-sar-apd-2/?pdf=view
[22] N. Chitnis, F. Karimi, A. Fallahi, S. Kuhn, and N. Kuster, "Tracable absorbed power density assessment system in the 28 GHz band," in *Proc. BioEM*, Oxford, U.K., Jun. 2023, pp. 4–5.
[23] M. Ziane, M. Zhadobov, and R. Sauleau, "High-resolution technique for near-field power density measurement accounting for antenna/body coupling at millimeter waves," *IEEE Antennas Wireless Propag. Lett.*, vol. 20, no. 11, pp. 2151–2155, Nov. 2021.
[24] M. Ziane, A. Boriskin, and M. Zhadobov, "Near-field power density mapping of close-to-body low-power mmWave devices," *IEEE Antennas Wireless Propag. Lett.*, vol. 22, no. 10, pp. 2347–2351, Oct. 2023.
[25] M. Ziane, M. Zhadobov, and R. Sauleau, "Multi-physics technique for absorbed power density measurement above 6 GHz," in *Proc. BioEM*, Nagoya Japan, Jun. 2022, pp. 647–651.
[26] C. Scott, *The Spectral Domain Method in Electromagnetics*. Norwood, MA, USA: Artech House, 1989.
[27] S. Gabriel, R. W. Lau, and C. Gabriel, "The dielectric properties of biological tissues: II. Measurements in the frequency range 10 Hz to 20 GHz," *Phys. Med. Biol.*, vol. 41, no. 11, pp. 2251–2269, Nov. 1996.
[28] A. R. Guraliuc, M. Zhadobov, O. De Sagazan, and R. Sauleau, "Solid phantom for body-centric propagation measurements at 60 GHz," *IEEE Trans. Microw. Theory Techn.*, vol. 62, no. 6, pp. 1373–1380, Jun. 2014.
[29] D. M. Pozar, *Microwave Engineering*. 4th ed. Hoboken, NJ, USA: Wiley, 2012.
[30] S. Gregson, J. McCormick, and C. Parini, "Principles of planar near-field antenna measurements," Inst. Eng. Technol., Michael Faraday House, Six Hills Way, U.K., IET, Tech. Rep. 53, 2007.
[31] *Measurement Procedure for the Assessment of Specific Absorption Rate of Human Exposure to Radio Frequency Fields From Hand-Held and Bodyworn Wireless Communication Devices—Human Models, Instrumentation and Procedures (Frequency Range of 4 MHz to 10 GHz)*, Standard IEC/IEEE 62209-1528, Oct. 2020.
[32] S. Omi, K. Sasaki, and K. Wake, "Performance analysis of incident power density evaluation by inverse source method for compliance assessment at quasi-millimeter and millimeter wave bands," *IEEE Trans. Electromagn. Compat.*, vol. 63, no. 5, pp. 1649–1657, Oct. 2021.
[33] K. Sasaki, K. Li, J. Chakarothai, T. Iyama, T. Onishi, and S. Watanabe, "Error analysis of a near-field reconstruction technique based on plane wave spectrum expansion for power density assessment above 6 GHz," *IEEE Access*, vol. 7, pp. 11591–11598, 2019.
[34] B. Xu et al., "Investigation of planar near-field measurement of millimeter-wave antenna for 5G application," in *Proc. Int. Symp. Antennas Propag. (ISAP)*, Okinawa, Japan, 2016, pp. 600–601.
[35] *Uncertainty of Measurement—Part 3: Guide to the Expression of Uncertainty in Measurement*, Standard ISO/IEC Guide 98-3:2008, 1995.
[36] P. D. Hislop and I. M. Sigal, *Introduction to Spectral Theory: With Applications to Schrödinger Operators*. New York, NY, USA: Springer, 1996.